View metadata, citation and similar papers at core.ac.uk

brought to you by CORE

provided by Brunel University Research Archive

SURFACE CHEMISTRY

Electrochemically induced phase separation and in situ formation of mesoporous structures in ionic liquid mixtures

Abhishek Lahiri[1]*, Niklas Behrens[1], Giridhar Pulletikurthi[1], Arik Yochelis[2,3], Edwin Kroke[4], Tong Cui[1], Frank Endres[1]*

Copyright © 2018 The Authors, some rights reserved; exclusive licensee American Association for the Advancement of Science. No claim to original U.S. Government Works. Distributed under a Creative Commons Attribution NonCommercial License 4.0 (CC BY-NC).

Liquid-liquid phase separation is mainly dependent on temperature and composition. Electric fields have also been shown to influence demixing of binary liquid mixtures. However, a puzzling behavior that remains elusive is the electric field–induced phase separation in ion-containing solvents at low voltages, as predicted by Tsori and Leibler. Here, we report the first experimental study of such a phenomenon in ionic liquid–silane mixtures, which not only results in phase separation at the electrode-electrolyte interface (EEI) but also is accompanied by deposition of porous structures of micrometer size on the electrode. This multiscale phenomenon at the EEI was found to be triggered by an electrochemically induced process. Using several analytical methods, we reveal the involved mechanism in which the formation of new Si–N bonds becomes unstable and eventually decomposes into the formation of silane-rich and silane-poor phases. The deposition of porous structures on the electrode surface is therefore a realization of the silane-rich phase. The finding of an electrochemically induced phase separation not only brings a paradigm shift in understanding the EEI in ionic liquids but also provides alternative strategies toward designing porous surfaces.

INTRODUCTION

Phase separation in binary mixtures near an electrode surface depends on wettability, surface geometry, temperature, and chemical composition (*1*–*4*). By controlling the solid-liquid interface, the development of nanostructured surfaces and self-organized patterned structures was shown to be possible (*5*–*8*). Intriguingly, it was shown over a decade ago that, for aqueous polymeric solutions, electric fields can change the demixing temperature (*9*–*11*). It was also predicted that, in ion-containing solvents, lateral phase separation can take place near the solid-liquid interface (*12*). Besides phase separation, in ion-containing solvents, electric fields can also trigger electrochemical reactions. For example, in electroplating metals and alloys, by controlling the charge and mass transfer processes of metal ions, large nanostructure electrodes with enhanced active surface areas, such as honeycomb-like patterns, can be formed from aqueous electrolytes (*13*).

In contrast, the electrode-electrolyte interface (EEI) in highly concentrated and solvent-free electrolytes, such as ionic liquids (ILs), often exhibits a qualitatively distinct multilayered structure (*14*, *15*). In addition, far from the solid-liquid interface region, the electrostatic forces prohibit coarsening of polar domains (*16*), and finite length scale self-organized nanostructure is observed in ILs (*17*) and ion-containing polymers (*18*). To date, the mechanistic rationale has been devoted to reactions and transport of ions to and at the EEI, ignoring any emerging phenomena that may occur at the EEI and the bulk electrolyte.

Here, we experimentally demonstrate electrochemically driven phase separation by spinodal decomposition near the EEI of an IL composition comprising 1-butyl-1-methylpyrrolidinium trifluoromethanesulfonate ($[Py_{1.4}]TfO$) with two different silanes of tetrakis(ethylmethylamino)silane (hereafter referred to as silane A) and tetrakis(dimethylamino)silane (hereafter referred to as silane B). We show not only that this phase separation forms via spinodal decomposition but also that the accompanied and competing deposition of Si introduces a distinct and relatively simple road map to synthesize self-assembled macroporous structures.

RESULTS AND DISCUSSION

To understand the thermal mechanisms for phase separation symmetry breaking, we seek first the temperature-induced phase changes. For this purpose, we use differential scanning calorimetry (DSC) measurements. Upon heating, we observe a solid-state phase transition, followed by melting of IL and IL + silane B, at −30° and ~2°C, respectively, while for IL + silane A, we observe only a melting point (see top curves in Fig. 1, A and B). Upon cooling (bottom curves), we observe only a crystallization peak for both cases. The absence of slope change or additional peaks below 95°C indicates that, in both systems, spinodal decomposition cannot be simply triggered by temperature. Similar results were also obtained for IL containing 0.1 M silane A and silane B, as seen in fig. S1.

Next, to assess the influence of an electric field above the melting point (at 23°C), we used cyclic voltammetry (CV) on polycrystalline Au. Figure 2 (A and B) shows that, in the absence of silanes in the cathodic regime, the increase in negative current from −3 V versus Pt is related to the decomposition of the $[Py_{1.4}]^+$ cation. Upon the addition of silane A or silane B, reduction peaks are observed in the cathodic regime at ~−2.2 V (Fig. 2, A and B), and, upon further scanning in toward negative voltage, a sharp increase in negative current at ~−2.7 V is seen, which indicates early decomposition of the $[Py_{1.4}]^+$. The low magnitude of the reduction currents (25 to

[1]Institute of Electrochemistry, Clausthal University of Technology, Arnold Sommerfeld Str. 6, D-38678, Clausthal-Zellerfeld, Germany. [2]Department of Solar Energy and Environmental Physics, Swiss Institute for Dryland Environmental and Energy Research, Blaustein Institutes for Desert Research (BIDR), Ben-Gurion University of the Negev, Midreshet Ben-Gurion 8499000, Israel. [3]Department of Physics, Ben-Gurion University of the Negev, Be'er Sheva 8410501, Israel. [4]Institute of Inorganic Chemistry, Technische Universität Bergakademie Freiberg, D-09599 Freiberg, Germany.
*Corresponding author. Email: abhishek.lahiri@tu-clausthal.de (A.L.); frank.endres@tu-clausthal.de (F.E.)

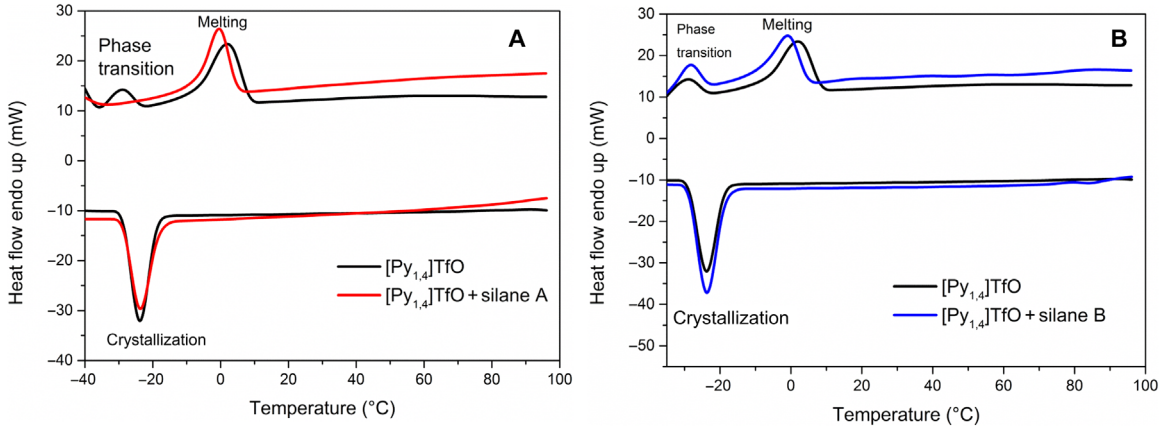

Fig. 1. DSC of silane A and B. DSC of (**A**) 0.05 M silane A in $[Py_{1,4}]TfO$ (**B**) 0.05 M silane B in $[Py_{1,4}]TfO$.

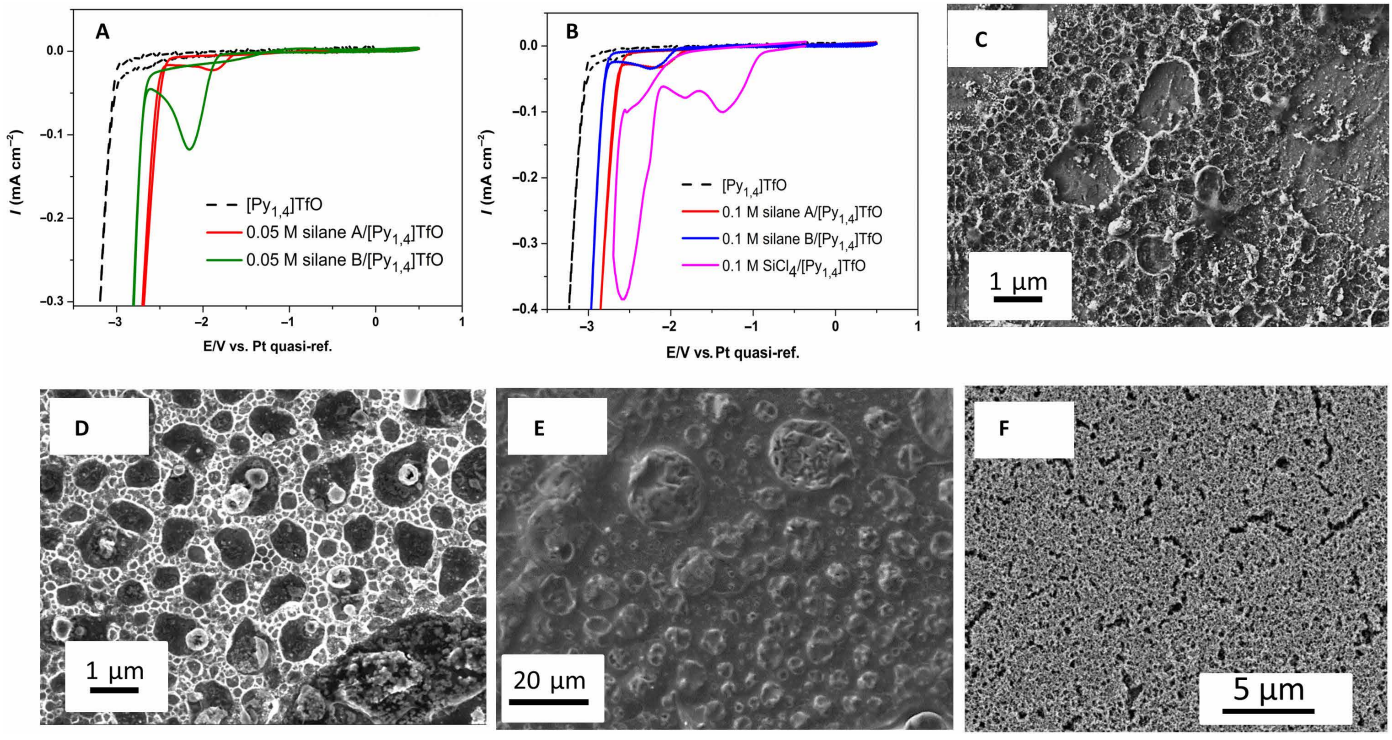

Fig. 2. CV and microstructure of the deposit. (**A** and **B**) CVs of pure $[Py_{1,4}]TfO$, 0.05 and 0.1 M silane A/$[Py_{1,4}]TfO$, silane B/$[Py_{1,4}]TfO$, and 0.1 M $SiCl_4$/$[Py_{1,4}]TfO$ on Au electrodes. (**C** and **D**) Scanning electron microscopy (SEM) of the Si-containing electrodeposit from 0.05 M silane B/$[Py_{1,4}]TfO$ and 0.1 M silane B/$[Py_{1,4}]TfO$ after applying pulsed deposition for 3 hours on Au. (**E**) SEM of the electrodeposit obtained on highly oriented pyrolytic graphite (HOPG) by applying a constant current (0.03 mA cm^{-2}) from 0.1 M silane A/$[Py_{1,4}]TfO$ for 8 hours. (**F**) SEM of electrodeposited silicon from 0.1 M $SiCl_4$/$[Py_{1,4}]TfO$ on Au at a constant potential of −2.2 V for 1 hour.

100 µA cm^{-2}) for both 0.05 and 0.1 M silane concentrations indicates that they are related to adsorption/interfacial processes at the EEI. It is observed that, upon increasing the silane B concentration, a decrease in current at −2.2 V occurs (Fig. 2B). To understand the suppression in the reduction peak, we performed in situ atomic force microscopy (AFM) with 0.05 and 0.1 M silane B in the IL (figs. S2 and S3). It is evident from figs. S2 and S3 that the interfacial processes differ upon increasing the concentration of silane B in $[Py_{1,4}]TfO$. With a 0.05 M concentration of silane B in $[Py_{1,4}]TfO$, a double-layer structure is observed at open-circuit potential (OCP) with a separation of 0.6 nm (fig. S2A), which increases to two layers upon changing the potential to −1.5 V (fig. S2D) and changes back to a double-layer structure at −2.0 V (fig. S2E). In comparison, with 0.1 M silane B, three solvation layers at a separation of 0.9, 1.9, and 2.9 nm are observed at OCP (fig. S3A) which, upon changing the potential to −2.0 V, increases to four solvation layers. This indicates that the composition at the EEI changes with increase in silane B concentration and potential. In addition, the forces required to rupture the solvation layers are higher for 0.1 M silane B than for 0.05 M silane B, which suggests a stronger

interaction of the silane B–IL species with the electrode surface. Therefore, the decrease in current observed in 0.1 M silane B in the IL can be attributed to different (strong) adsorption of silane B–IL species at the EEI compared to that formed by 0.05 M silane B in the IL.

In contrast, upon the addition of 0.1 M $SiCl_4$ in $[Py_{1.4}]TfO$ (Fig. 2B), three reduction peaks are seen in the cathodic regime. The first two peaks at −1.3 and −1.7 V are related to adsorption/interfacial process, while the reduction process commencing at −1.9 V is related to the deposition of silicon (*19*). The current observed is much higher than that of silanes in the IL, which indicates that the deposition process is different in presence of $SiCl_4$.

To identify the characteristics of the adsorption in silane-containing ILs, we performed first a pulsed deposition at −2.0 and +0.2 V for 0.5 s each for 3 hours using 0.05 and 0.1 M silane B/$[Py_{1.4}]TfO$. Figure 2 (C and D) shows Si-containing deposits with a porous network deposit representing a spinodal decomposed structure for both 0.05 and 0.1 M silane B/$[Py_{1.4}]TfO$, respectively. Notably, a similar porous structure was obtained from silane A/$[Py_{1.4}]TfO$ electrolyte when applying a constant potential/current on both Au (fig. S4, A to D) and Cu (fig. S4, E and F) substrates at different potentials. As silicon can alloy with Au and then segregate by spinodal decomposition as observed in the case of electrodeposition of Cd and Zn from $AlCl_3$-containing ILs (*20*, *21*), we also performed experiments on HOPG using silane A/$[Py_{1.4}]TfO$ as the electrolyte. Circular porous islands on HOPG are shown in Fig. 2E, and the energy-dispersive x-ray (EDX) maps in fig. S5 (A and B) show domains of C and Si, respectively.

In comparison, upon using $SiCl_4$ as the precursor, the porosity is significantly reduced (Fig. 2F), which confirms that the mechanism of deposition is different upon changing the precursors. The x-ray photoelectron spectra (XPS) of the deposit obtained from silane-containing IL confirmed the presence of SiO and SiO_2 (fig. S6), which occurs because of a surface oxidation of the deposited silicon-containing material during transfer to the XPS chamber. Thus, from the above results, the porous deposits appear to be independent of the electrode material used, indicating imprinting by processes that occur in the electrolyte. In what follows, we show that the porous morphology is obtained by a phase separation that happens near the electrode/electrolyte surface due to lateral spinodal decomposition.

To uncover the spinodal decomposition process in the liquid phase, we probed the EEI using in situ optical microscopy, in situ AFM, and Raman spectroscopy under potential control. Initial optical microscopy experiments were performed on a Au electrode with a droplet of the electrolyte. Imaging shows that circular droplets (see red arrows in fig. S7) have formed on the electrode without complete demixing of the electrolyte during the first 60 s, and the size was found to increase with time. To identify the formed droplets as distinct phases as compared to the background, we used a Au mesh electrode under a pulsed deposition process that is similar to that reported in Fig. 1. The optical images in Fig. 3 (A to C) also showed similar droplet formation and growth over time. However, after 110 min of the experiment (see Fig. 3C), the size of the droplet reached macroscopic scale (about 500 μm) and was found to be stable even after removing the electric field. The latter indicates that

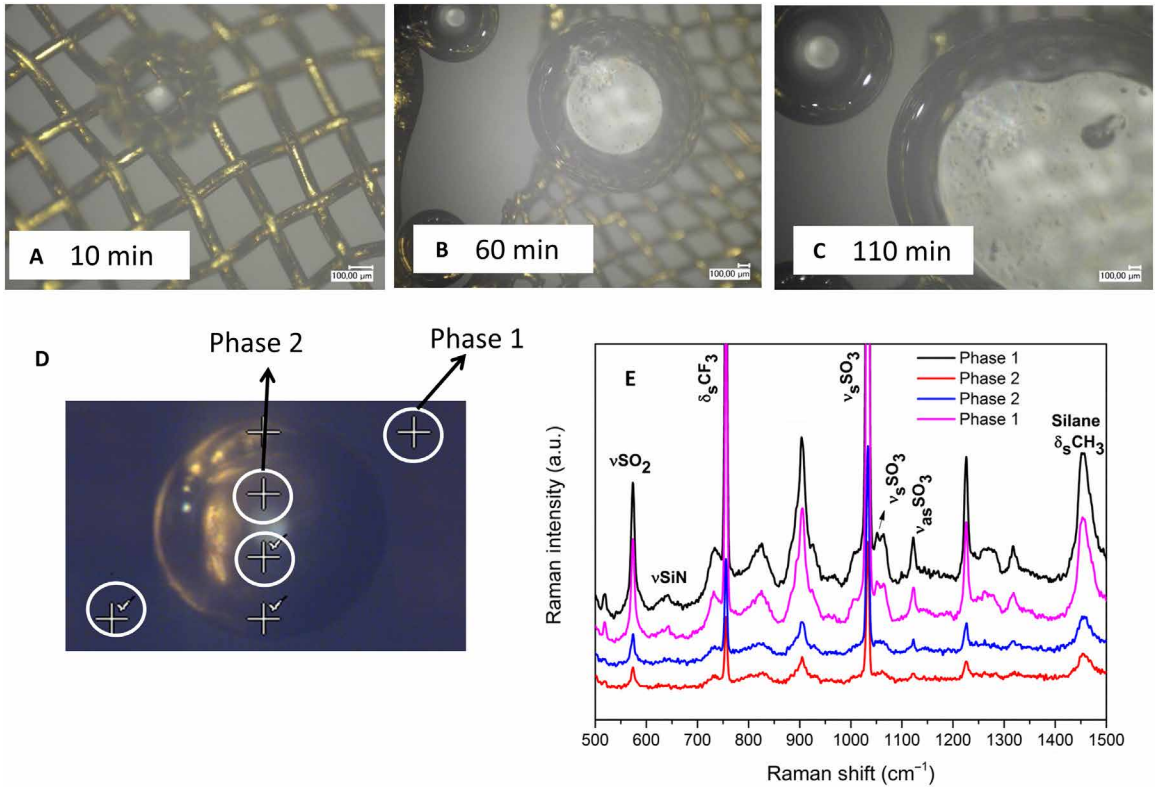

Fig. 3. Optical image and Raman spectroscopy. Optical image of a droplet on a Au mesh electrode in 0.05 M silane B/$[Py_{1.4}]TfO$ under pulsed deposition (−2.0 and +0.2 V for 0.5 s each) for (**A**) 10 min, (**B**) 60 min, and (**C**) 110 min. (**D**) Optical microscopy image of a droplet and marked points (represented by "+") where Raman spectroscopy measurement was performed. (**E**) Micro-Raman spectroscopy of the droplet (phase 2) and outside the droplet (phase 1) between 500 and 1500 cm^{-1}. a.u., arbitrary units.

the droplet composition and the surrounding can be regarded as two distinct phases. Notably, examination of the Au mesh electrode at the end of the experiment showed a black appearance, which indicates Si-containing material deposited during the liquid phase separation process.

To identify the chemical composition of the two liquid phases and relate them to Si deposits, we used micro-Raman spectroscopy to probe the droplet and background content, as shown in Fig. 3D. The spectra of the phases (Fig. 3E) taken at different points (marked by white circles in Fig. 3D) demonstrate that the composition of the droplet is different from the liquid present outside. The background liquid (hereafter referred to as phase 1) shows a υSiN peak at 640 cm^{-1} due to the presence of silane B (*22*). In contrast, for the droplet (hereafter referred to as phase 2), the υSiN peak is missing. Although some peaks related to silane B such as $\delta_s CH_3$ are present at 1450 cm^{-1}, it is evident from the spectra in Fig. 2E that the composition of the droplet (phase 2) relates to a silane-poor region from which the porous silicon-containing deposit must have deposited by a charge transfer process.

Last, to connect the spinodal decomposition processes with the Si deposit, we probed the EEI using in situ AFM and Raman spectroelectrochemistry. From in situ AFM, as the AFM cantilever approaches the Au(111) surface in the IL containing silane B at OCP, a repulsive force at 1.9 nm is incurred (Fig. 4A), followed by a sudden jump in force. Similar repulsive forces are observed at 1.05 and 0.35 nm before contact with the electrode. These peaks in the force-separation curves arise due to rupturing of the solvation layers in ILs (*23*). Repeated experiments show that these repulsive forces are quite stable at OCP. Upon comparing the force-separation curves with that of pure $[Py_{1.4}]TfO$ (*24*), a change in the innermost layer of ~0.2 nm is seen, which is due to the presence of silane B in the IL. Upon applying a pulsed deposition for 1 hour (Fig. 4B), random changes and, sometimes, loss of the solvation layer are observed, and the forces vary between 2 and 8 nN, which suggests a change in the composition at the EEI. As we do not see any changes at OCP, we can attribute the changes occurred during pulse deposition to spinodal decomposition, which triggers the liquid phase separation and deposition of porous Si-containing material.

With time, changes in the solvation layers are evident, as shown in Fig. 4 (C and D) and fig. S8 (A and B). Between 2 and 3 hours, the innermost layer shuttles between 0.3 and 0.5 nm, which can be related to a switch between silane B/$[Py_{1.4}]TfO$ (silane-rich) and pure $[Py_{1.4}]TfO$ (silane-poor) at the interface. The forces also vary

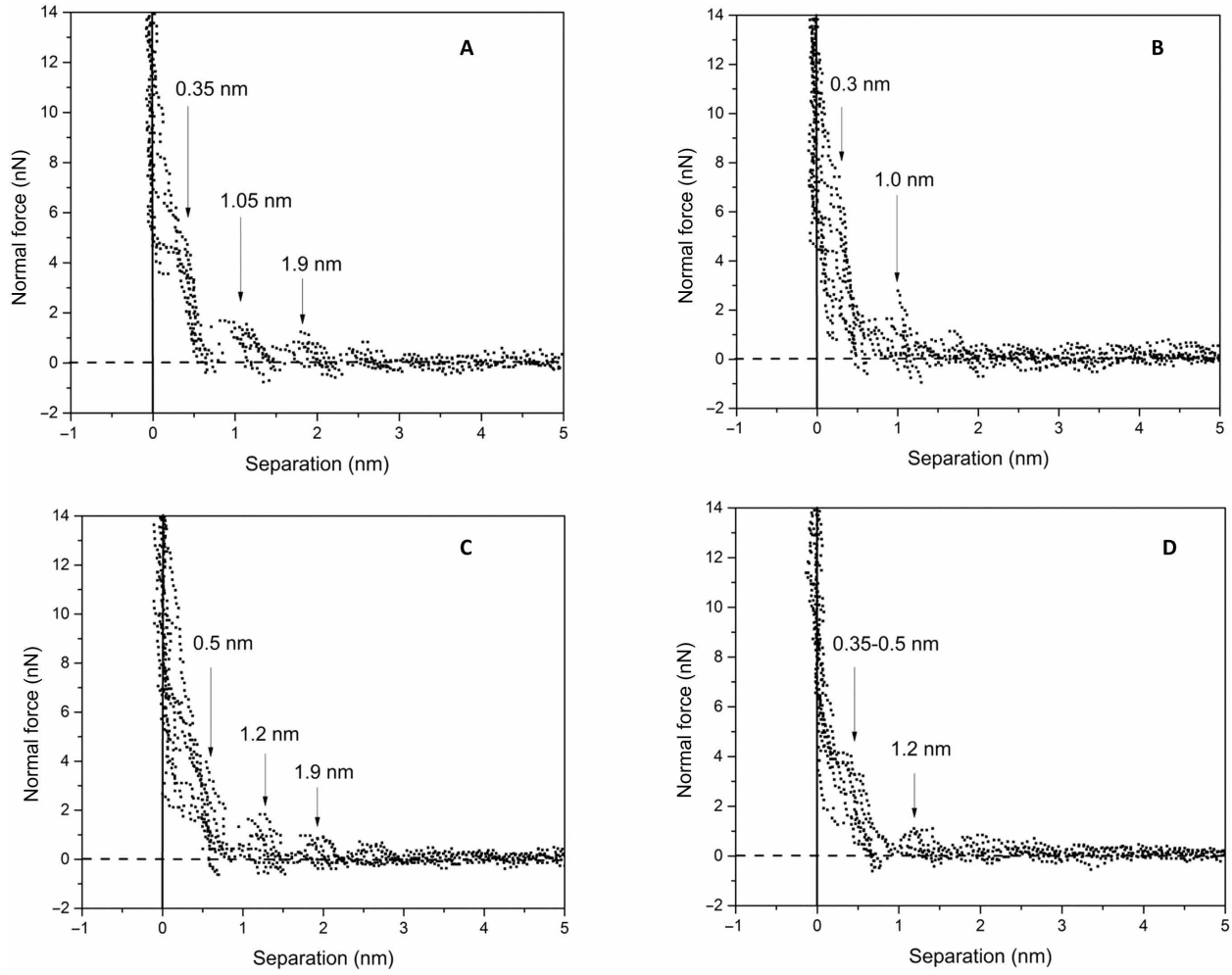

Fig. 4. Atomic force spectroscopy at various time intervals. (**A**) AFM force-separation curves of 0.05 M silane B/$[Py_{1.4}]TfO$ at OCP (**B**) after 1 hour (−2.0 and +0.2 V for 0.5 s each), (**C**) after 2 hours, and (**D**) after 2.5 hours of pulsed deposition.

within 0 to 3 nN (Fig. 4, C and D, and fig. S8, A and B), which can be associated with the deposition of silicon-containing material and the difference in the adsorption of the electrolyte due to spinodal decomposition. In situ Raman spectroelectrochemistry of the IL-containing silane B was also used to understand the changes at the EEI. Random changes for υSiN peaks at 600 cm^{-1} and $υSO_2$ peaks at 573 cm^{-1} are evident (fig. S9, A and B), which suggests a change in the electrolyte composition at the EEI. Furthermore, in the regions corresponding to υSiN peaks at ~640 and 658 cm^{-1} (see dashed lines in fig. S9A), with applied pulsed potential, new Si–N bonds appear and disappear, which is a clear evidence of formation of an unstable composition.

This unstable composition might allow the spinodal decomposition to take place, which also results in the changes observed from the in situ AFM measurements in Fig. 4. Moreover, the notable changes in the spectra between 260 and 420 cm^{-1} (fig. S10) further clarify the compositional changes at the EEI. Consequently, the results indicate that the presence of an electrical field (electrode potential) induces a structural change at the EEI, leading to the formation of an unstable silane structure (Fig. 5). This unstable structure spontaneously undergoes spinodal decomposition and results in phase separation in the liquid with almost simultaneous charge transfer process taking place at the EEI that results in deposition of spinodal-like porous silicon-containing material on the electrode, as shown in Fig. 5, thus representing a multiscale phenomenon of ILs at the interface.

CONCLUSION

To conclude, we report on a novel electrochemically induced lateral phase separation (spinodal decomposition) process that starts in the electrolyte near the electrode surface and proceeds along with almost simultaneous deposition of porous silicon-containing material by a charge transfer process. This mechanism differs from typically observed spinodal decomposition processes wherein, unlike temperature, applied potential results in the formation of three phases. This technique not only opens up new vistas to fundamental understanding of liquid-liquid phase separation in concentrated electrolytes but also can be applied for developing porous surfaces with relevance to catalysis, energy storage, and sensing.

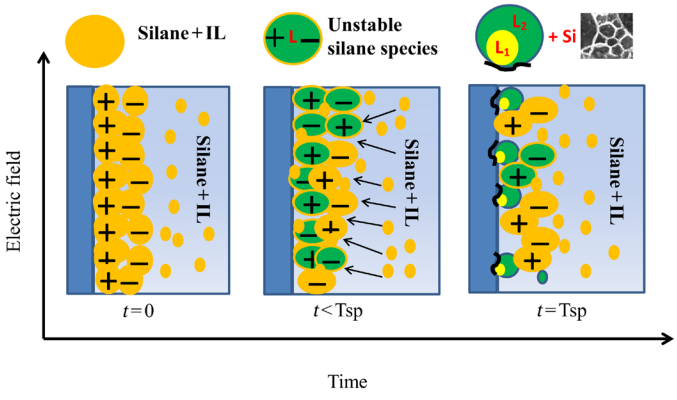

Fig. 5. Illustration of phase separation and mesoporous deposition. Schematic diagram summarizing the results, where Tsp is the time at spinodal decomposition, L_1 is the silane-rich phase, and L_2 is the silane-poor phase.

MATERIALS AND METHODS

$[Py_{1,4}]TfO$ was purchased in the highest available quality from IoLiTec (Germany) and was used after drying under vacuum at 100°C to remove the water content to below 2 parts per million (ppm). Both silane A and silane B were synthesized in the group of E.K. at Technische Universität Bergakademie, Freiberg according to literature (*25*–*27*). Polycrystalline Au, Cu, and HOPG were used as working electrodes. The Au electrode, as well as the Pt wires, which were used as counter electrode (CE) and quasi–reference electrode (RE), were heated in a hydrogen flame to remove any surface impurities. A copper plate was cleaned in a mixture of acetone and isopropanol in an ultrasonic bath before the experiment. For HOPG, a few layers from the top were removed using a Scotch tape. The electrochemical cell was made of polytetrafluoroethylene (PTFE) and clamped over a PTFE-covered Viton O-ring onto the substrate, providing a geometric area of 0.3 cm^2. The Teflon cell and the O-ring were cleaned in a mixture of 50:50 volume % of concentrated H_2SO_4 and H_2O_2 (35%), followed by refluxing in distilled water.

The electrochemical measurements were performed in an Ar-filled glove box with water and oxygen contents of below 0.5 ppm (OMNI-LAB from Vacuum Atmospheres) by using a VersaStat II (Princeton Applied Research) potentiostat/galvanostat controlled by PowerSuite software. The scan rate during CV was set to 10 mV s^{-1}. For pulsed deposition, a potential of −2.0 and +0.2 V was applied. Constant potential deposition was performed at various current densities. For SEM (JSM-7610F, JEOL) and EDX analysis, the electrodeposited samples were cleaned with acetonitrile inside of the glove box.

DSC was performed in Mettler Toledo DSC 1 at a heating and cooling rate of 10 K min^{-1}. XPS measurements were obtained using an ultrahigh vacuum apparatus with a base pressure of below 1×10^{-10} hPa. The sample was irradiated using the Al Kα line (photon energy of 1486.6 eV) of a nonmonochromatic x-ray source (DAR 400, Omicron). Electrons emitted were detected by a hemispherical analyzer (EA 125, OMICRON) at an angle of 45° to the surface normal with a calculated resolution of 0.83 eV for detail spectra and 2.07 eV for survey spectra. All XPS results were displayed as a function of the binding energy with respect to the Fermi level.

Raman spectra were recorded with a Raman module (Ram II) Bruker VERTEX 70v (Nd:YAG, 1064 nm) with a Ge detector. Raman spectroelectrochemistry was performed in an ALS spectroelectrochemical cell with a path length of 1 mm. A Au mesh electrode (80 mesh with ~42-mm^2 dimension) was used as the working electrode, with Pt wires as CE and RE. The electrolyte was sealed in the spectroelectrochemical cell inside of the glove box, and the spectra were obtained at a resolution of 2 cm^{-1}. For optical microscopy, the working electrode was a Au mesh or a screen-printed Au electrode (250 AT, Metrohm). The same Raman spectroelectrochemical cell was used for optical microscopic imaging (Keyence Digital Microscope, VHX-100D).

Force-distance curves were collected using a Molecular Imaging PicoPlus AFM in contact mode. A silicon SPM-sensor from NanoWorld with a spring constant of 6 N/m was used for all the experiments. Au(111) was used as the working electrode, with two Pt wires as the CE and RE. Before each experiment, the electrochemical cell and Pt wires were cleaned with isopropanol in an ultrasonic bath for 5 min and then annealed in a hydrogen flame to red glow to remove any possible contaminations.

SUPPLEMENTARY MATERIALS

Supplementary material for this article is available at http://advances.sciencemag.org/cgi/content/full/4/10/eaau9663/DC1

Fig. S1. Differential scanning calorimetry of 0.1 M silane A and silane B in [$Py_{1,4}$]TfO.
Fig. S2. AFM force-separation curves of 0.05 M silane B in [$Py_{1,4}$]TfO at different potentials.
Fig. S3. AFM force-separation curves of 0.1 M silane B in [$Py_{1,4}$]TfO at different potentials.
Fig. S4. Scanning electron microscopy of the electrodeposit on Au and Cu at different potentials and current densities.
Fig. S5. Energy dispersive x-ray map of C and Si on HOPG.
Fig. S6. XPS survey spectra and detailed spectra of the electrodeposit on Cu.
Fig. S7. Optical image of phase separation on gold electrode under pulsed deposition at various time intervals.
Fig. S8. AFM force-separation curves of 0.05 M silane B/[$Py_{1,4}$]TfO under pulsed deposition at various time intervals.
Fig. S9. In situ Raman spectroelectrochemistry of 0.05 M silane B/[$Py_{1,4}$]TfO under pulsed conditions at various time intervals between 540 and 720 cm^{-1}.
Fig. S10. Raman spectroelectrochemistry of 0.05 M silane B/[$Py_{1,4}$]TfO under pulsed deposition at various time intervals between 260 and 420 cm^{-1}.

REFERENCES AND NOTES

1. C. Rascón, A. O. Parry, Geometry-dominated fluid adsorption on sculpted solid substrates. *Nature* **407**, 986–989 (2000).
2. K.-I. Murata, H. Tanaka, Impact of surface roughness on liquid-liquid transition. *Sci. Adv.* **3**, e1602209 (2017).
3. P. G. de Gennes, Wetting: Statics and dynamics. *Rev. Mod. Phys.* **57**, 827–863 (1985).
4. D. Bonn, D. Ross, Wetting transitions. *Rep. Prog. Phys.* **64**, 1085–1163 (2001).
5. A. M. Higgins, R. A. L. Jones, Anistropic spinodal dewetting as a route to self-assembly of patterned surfaces. *Nature* **404**, 476–478 (2000).
6. W. A. Lopes, H. M. Jaeger, Hierarchical self-assembly of metal nanostructures on diblock copolymer scaffolds. *Nature* **414**, 735–738 (2001).
7. K. Liu, X. Yao, L. Jiang, Recent developments in bio-inspired special wettability. *Chem. Soc. Rev.* **39**, 3240–3255 (2010).
8. P. J. Yoo, H. H. Lee, Evolution of a stress-driven pattern in thin bilayer films: Spinodal wrinkling. *Phys. Rev. Lett.* **91**, 154502 (2003).
9. A. Onuki, Electric-field effects in fluids near the critical point. *EPL* **29**, 611–616 (1995).
10. E. Schäffer, T. Thurn-Albrecht, T. P. Russell, U. Steiner, Electrically induced structure formation and pattern transfer. *Nature* **403**, 874–877 (2000).
11. R. Verma, A. Sharma, K. Kargupta, J. Bhaumik, Electric field induced instability and pattern formation in thin liquid films. *Langmuir* **21**, 3710–3721 (2005).
12. Y. Tsori, L. Leibler, Phase-separation in ion-containing mixtures in electric fields. *Proc. Natl. Acad. Sci. U.S.A.* **104**, 7348–7350 (2007).
13. K. Krischer, N. Mazouz, P. Grauel, Fronts, waves, and stationary patterns in electrochemical systems. *Angew. Chem. Int. Ed.* **40**, 850–869 (2001).
14. R. Hayes, G. G. Warr, R. Atkin, Structure and nanostructure in ionic liquids. *Chem. Rev.* **115**, 6357–6426 (2015).
15. M. V. Fedorov, A. A. Kornyshev, Ionic liquids at electrified interfaces. *Chem. Rev.* **114**, 2978–3036 (2014).
16. A. Yochelis, M. B. Singh, I. Visoly-Fisher, Coupling bulk and near-electrode interfacial nanostructuring in ionic liquids. *Chem. Mater.* **27**, 4169–4179 (2015).
17. N. Gavish, I. Versano, A. Yochelis, Spacially localised self-assembly driven by electrically charged phase separation. *SIAM J. Appl. Dyn. Syst.* **16**, 1946–1968 (2017).
18. A. R. Khokhlov, E. E. Dormidontova, Self-organization in ion-containing polymer systems. *Phys. Usp.* **40**, 109–124 (1997).
19. G. Pulletikurthi, A. Lahiri, T. Carstens, N. Borisenko, S. Zein El Abedin, F. Endres, Electrodeposition of silicon from three different ionic liquids: Possible influence of the anion on the deposition process. *J. Solid State Electrochem.* **17**, 2823–2832 (2013).
20. J. Dogel, R. Tsekov, W. Freyland, Two-dimensional connective nanostructure of electrodeposited Zn on Au(111) induced by spinodal decomposition. *J. Chem. Phys.* **122**, 094703 (2005).
21. G.-B. Pan, W. Freyland, In situ STM investigation of spinodal decomposition and surface alloying during underpotential deposition of Cd on Au(111) from an ionic liquid. *Phys. Chem. Chem. Phys.* **9**, 3286–3290 (2007).
22. D. G. Anderson, J. Armstrong, S. Cradock, Preparation, properties, and vibrational spectra of some (dimethylamino)halogenosilanes. *J. Chem. Soc. Dalton Trans.* **0**, 3029–3034 (1987).
23. N. Borisenko, A. Lahiri, G. Pulletikurthi, T. Cui, T. Carstens, J. Zahlbach, R. Atkin, F. Endres, The Au(111)/IL interfacial nanostructure in the presence of precursors and its influence on the electrodeposition process. *Faraday Discuss.* **206**, 459–473 (2018).
24. A. Lahiri, M. S. Ghazvini, G. Pulletikurthi, T. Cui, V. Klemm, D. Rafaja, F. Endres, Modification of the electrolyte/electrode interface for the template-free electrochemical synthesis of metal nanowires from ionic liquids. *J. Phys. Chem. Lett.* **9**, 1272–1278 (2018).
25. G. Kannengiesser, F. Damm, Preparation of several tetra(dialkylamino)silanes. *Bull. Soc. Chim. Fr.* **7**, 2492–2495 (1967).
26. C. Banerjee, C.R. Wade, A. Soulet, G. Jursich, J. McAndrew, J. A. Belot, Direct synthesis and complete characterisation of halide-free tetrakis(dialkylamino)silanes. *Inorg. Chem. Commun.* **9**, 761–763 (2006).
27. C. Wiltzsch, J. Wagler, G. Roewer, E. Kroke, Sol-gel analogous aminolysis-ammonolysis of cholorosilanes to chlorine-free Si/(C)/N-materials. *Dalton Trans.* **0**, 5474–5477 (2009).

Acknowledgments

Funding: There was no project funding for this work. **Author contributions:** F.E. conceived the idea. F.E. and A.L. recognized the spinodal structure. A.L. planned and performed subsequent in situ Raman and optical microscopy experiments to prove the phenomena. N.B. performed the electrochemical experiments and characterization of the deposits. T.C. performed the in situ AFM experiments. E.K. synthesized the Silane liquids. A.L., G.P., A.Y., and F.E. discussed and interpreted the results and wrote the manuscript. **Competing interests:** The authors declare that they have no competing interests. **Data and materials availability:** Supplementary Material is available for this paper and includes DSC measurements, additional SEM, optical microscopy, AFM, and Raman spectroscopy results. All data needed to evaluate the conclusions in the paper are present in the paper and/or the Supplementary Materials. Additional data related to this paper may be requested from the authors.

Submitted 1 August 2018
Accepted 19 September 2018
Published 26 October 2018
10.1126/sciadv.aau9663

Citation: A. Lahiri, N. Behrens, G. Pulletikurthi, A. Yochelis, E. Kroke, T. Cui, F. Endres, Electrochemically induced phase separation and in situ formation of mesoporous structures in ionic liquid mixtures. *Sci. Adv.* **4**, eaau9663 (2018).